A Refined Calibration Procedure of Two-Channel Sun Photometers to Measure Atmospheric Precipitable Water at Various Antarctic Sites

CLAUDIO TOMASI AND BOYAN PETKOV

Institute of Atmospheric Sciences and Climate (ISAC), Consiglio Nazionale delle Ricerche, Bologna, Italy

ELENA BENEDETTI

Institute of Acoustics "O. M. Corbino" (IDAC), Consiglio Nazionale delle Ricerche, Roma Tor Vergata, Italy

LUCA VALENZIANO

Institute of Space Astrophysics and Cosmic Physics, INAF, Bologna, Italy

ANGELO LUPI, VITO VITALE, AND UBALDO BONAFÉ

Institute of Atmospheric Sciences and Climate (ISAC), Consiglio Nazionale delle Ricerche, Bologna, Italy

(Manuscript received 18 December 2006, in final form 15 June 2007)

ABSTRACT

Two-channel sun photometers can be easily employed at Antarctic sites, where harsh environmental conditions prevail, to carry out measurements of precipitable water W. In the very dry air conditions observed in the Antarctic atmosphere, water vapor does not produce strong absorption features along the sun path. Therefore, these instruments need to be calibrated using analytical forms different from the square root regime, which can be determined by simulating the output voltages measured at Antarctic sites, for the spectral near-IR curves of extraterrestrial solar irradiance, instrumental responsivity parameters, and atmospheric transmittance, relative to various measurement periods. For this purpose, average models of the Antarctic atmosphere from the ground level up to the 30-km altitude were considered for different solar zenith angles and relative humidity conditions. The ratios between the output voltages simulated in the band and window channels were plotted as a function of total water vapor content C_w, for each site and each period, to define the best-fit calibration curves, which were subsequently normalized to the field measurements to take into account the aging effects on the filter transmission characteristics. Each of the five calibration curves was found to present a slope coefficient decreasing gradually with C_w from values higher than 0.8 to about 0.6. Using these curves, measurements of W were obtained, which differ appreciably at both sea level and high-altitude sites from those given by the square root calibration curves, avoiding large overestimation errors of 10%–40% at the high-altitude sites and underestimation errors of 5%–15% at the sea level site.

1. Introduction

Among the numerous minor atmospheric gases, water vapor is known to have very important effects on atmospheric opacity, which are less marked than elsewhere at the high-altitude Antarctic sites (South Pole, Dome C), where the columnar content of water vapor is usually low, because of the extremely cold and dry air conditions (Bally 1989; Burton et al. 1994; Bussmann et al. 2005). Astrophysical observations performed at these high-altitude sites over the Antarctic Plateau, within the infrared (2–20 μm) and/or millimetric (450 μm–2 mm) wavelength range, can provide a wealth of information (early stages of stellar evolution, infrared galaxies, cosmic structures at high redshift, properties of interstellar medium at low temperatures) of the same quality as analogous measurements taken from spaceborne platforms [satellites, stratospheric balloons, airplanes; see the Herschel Web site (http://sci.esa.int/science-e/www/area/index.cfm?fareaid=16), the Spitzer

Corresponding author address: Claudio Tomasi, Institute of Atmospheric Sciences and Climate (ISAC), Consiglio Nazionale delle Ricerche, via Gobetti 101, I-40129 Bologna, Italy.
E-mail: c.tomasi@isac.cnr.it

DOI: 10.1175/2007JTECHA952.1

Web site (http://www.spitzer.caltech.edu/spitzer/index.shtml), and the Stratospheric Observatory for Infrared Astronomy (SOFIA) Web site (http://www.sofia.usra.edu/index.html)], high-altitude desert sites [Atacama in Chile; see the Atacama Large Millimeter Array (ALMA) Web site (http://www.eso.org/projects/alma)], or volcano summits (Mauna Kea, in the Hawaii Islands).

The opening of a French–Italian all-year-round station at Dome C (75°06′S, 123°21′E, 3250 m MSL) in 2005 presented many new opportunities for research, including studies in atmospheric sciences, astronomy, and satellite data validation (Tomasi et al. 2006; Calisse et al. 2004; Walden et al. 2006). Extensive site testing measurements have been performed in recent years to asses the suitability of atmospheric transparency conditions at Dome C for astronomical observations (Valenziano and Dall'Oglio 1999; Lawrence et al. 2004; Aristidi et al. 2005). In particular, Valenziano et al. (1998) carried out a measurement campaign during the Antarctic Plateau Anisotropy Chasing Experiment in 1996/97 (APACHE96), which confirmed that the atmospheric opacity conditions at Dome C are such as to allow the regular performance of significant astronomical observations at submillimeter and millimeter wavelengths, not only during the austral summer but also in the winter season. They also showed that routine measurements of water vapor content in the atmospheric vertical column (briefly called precipitable water) are required to evaluate precisely the absorption effects due to atmospheric water vapor.

Additionally, measurements of precipitable water W can be very useful for validating upwelling radiance measurements provided by the Atmospheric Infrared Sounder (AIRS) at Dome C with interferometric ground-based measurements of upwelling and downwelling infrared radiance (Walden et al. 2006). Such preliminary activities indicated that the Antarctic Plateau is an ideal ground site for the calibration and validation of satellite data, since it presents in general homogeneous features of cold air, low atmospheric humidity, and cloud-free conditions over large areas.

Accurate and systematic measurements of W for astronomical studies are usually achieved using microwave radiometers or radiosondes. The former provide precise measurements of W, but their deployment involves high costs and great logistic effort (Westwater et al. 2001, 2003; Aonashi et al. 2004). Radiosounding data generally provide average values of W within the balloon flight range (sometimes equal to some tens of kilometers in Antarctica) and are commonly taken only a few times a day. Since large telescope facilities require a careful selection of the site to fully exploit the potential of the instruments, it is often necessary to compare precipitable water data from sites located a few kilometers from each other (more information is available online at the ALMA Web site: http://www.eso.org/projects/alma). Radiosoundings are not able to discriminate these details, while microwave radiometers are expensive and difficult to use at Antarctic Plateau sites. Therefore, portable two-channel sun photometers could be suitably employed for carrying out continuous measurements of W, with accuracy and reliability better than those achieved directly from radiosounding data. Such instruments generally have low costs and are easy to operate in harsh conditions, being transportable by backpack. However, the two-channel sun photometers most commonly used until now need to be carefully calibrated for measuring the low values of W normally observed at Antarctic sites.

Measurements of W were taken by Valenziano et al. (1998) at the Terra Nova Bay (TNB; 74°42′S, 164°06′E; 92 m MSL), Hercules Névé (HN; 73°06′S, 165°28′E; 2960 m MSL), and Dome C sites, during various field campaigns in the austral summer periods of 1993/94, 1994/95 and 1996/97, using a pair of portable two-channel sun photometers manufactured with more advanced optical and electronic components than those of the instrument designed by Tomasi and Guzzi (1974). The instruments of Valenziano et al. (1998) were calibrated at TNB through intercomparison tests performed with a Volz (1974) sun photometer on several austral summer days from 1993 to 1996. The values of W were found to vary mainly between 0.03 and 0.60 cm at TNB and between 0.02 and 0.18 cm at Dome C. At the latter site, a more limited range, from 0.04 to 0.15 cm, was determined by Tomasi et al. (2006), who analyzed a set of radiosounding measurements following the correction procedures of Wang et al. (2002) and Miloshevich et al. (2004, 2006) to remove the humidity dry bias and lag errors. Bearing these results in mind, the precipitable water values of Valenziano et al. (1998) were found to be underestimated to an extent varying between 10% and 22%. In fact, they were obtained by (i) analyzing directly the radiosounding data taken routinely at the TNB station, without using dry bias correction procedures, and (ii) using such underestimated values of W to determine the square root calibration curve of the sun-photometric ratio as a function of total water vapor content C_w,[1] expressed in terms of the ana-

[1] Total water vapor content C_w gives the measure of the overall volume occupied by the atmospheric water vapor distributed along the atmospheric slant path described by solar rays, this quantity being given by the integral of absolute humidity along the sun path, commonly measured in centimeters.

lytical form proposed by Volz (1974). Therefore, the estimates of Valenziano et al. (1998) were presumably affected by three different errors, because of the fact that 1) the sun-photometric ratios were not corrected by Valenziano et al. (1998) for the surface pressure conditions; 2) precipitable water was evaluated using a square root calibration curve determined on the basis of underestimated values of W, obtained directly from the original TNB radiosounding data, without dry bias corrections; and 3) precipitable water was determined using the Volz (1974) square root calibration curve, such a strong water vapor absorption regime law being inappropriate for use in the Antarctic atmosphere, as pointed out by Tomasi et al. (1990).

Therefore, considering the inadequacy of the square root calibration curves, it was decided to define more realistic analytical forms of the sun-photometric ratio calibration curve in the Antarctic atmosphere, using (i) radiative transfer codes to simulate the weak absorption by water vapor and (ii) the field measurements of sun-photometric ratio performed by Valenziano et al. (1998) to determine empirically some shape parameters of the calibration curves.

Before presenting the results of the simulation studies, it is useful to describe the basic concepts of the near-IR two-channel sun photometer technique, giving a measure of the water vapor absorption variability within the spectral range covered by the $\rho\sigma\tau$ water vapor band.

2. The two-channel sun photometer technique

The two-channel sun photometer technique consists basically of taking a pair of simultaneous direct solar irradiance measurements within two narrow spectral intervals centered at nearby wavelengths, the first usually chosen in the middle of a near-infrared water vapor band, and the second within a nearby transparency window of the solar spectrum. The $\rho\sigma\tau$ band covers the 0.91–0.98-μm wavelength range and is most commonly preferred for this application, since the direct solar irradiance measured at the ground within the wavelength interval of about 10-nm width covering the middle part of this water vapor band does not assume null values in all cases, even for rather high values of C_w (Gates 1956; Thome et al. 1992, 1994). Both side windows exhibit very weak absorption features, but the one on the short-wavelength side is generally preferred, since the silicon solar cells employed as sensors have higher and more uniform responsivity performances at these shorter wavelengths. Thanks to the choice of these narrow spectral channels, the ratio between the direct solar irradiance measurements taken within such band and window channels (hereinafter referred to as sun-photometric ratio) turns out to depend closely on C_w as a result of the relatively intense absorption due to the $\rho\sigma\tau$ band.

The direct solar irradiance measurements are extinguished not only by atmospheric water vapor but are also slightly affected by other atmospheric attenuation effects, such as (i) absorption by minor gases, giving negligible optical depths within the 0.86–0.96-μm wavelength range; (ii) Rayleigh scattering; and (iii) aerosol extinction. Rayleigh scattering optical depth assumes very close values at the two-channel peak wavelengths of about 0.87 and 0.94 μm, with differences evaluated to be smaller than 0.004 at TNB and 0.003 at the Dome C station, these estimates being inferred from the subarctic summer atmosphere Rayleigh scattering model (Tomasi et al. 2005). Aerosols yield values of optical depth (AOD) within the two channels, which vary appreciably from one day to another as a function of atmospheric turbidity conditions. For values of the Ångström exponent α ranging most frequently between 0.5 and 1.5 at TNB, associated with values of AOD generally lower than 0.05 at the 0.50-μm wavelength (Vitale and Tomasi 1990; Di Carmine et al. 2005), the difference ΔAOD was found to be in general lower than 0.002. Even lower values of ΔAOD are usually observed at the high-altitude sites on the Antarctic Plateau, causing relative errors smaller than 1% in the sun-photometric ratio measurements, for solar zenith angles (SZAs) $< 79°$.

Parameter C_w is usually measured as the product

$$C_w = m_w W, \tag{1}$$

where (i) m_w is the relative optical air mass for water vapor (Kasten 1966), determined as a function of the apparent solar zenith angle SZA, providing the measure of the relative "length" of the sun path; and (ii) W is the columnar volume content of water vapor, defined as the integral of absolute humidity $q(z)$ along the vertical atmospheric path.

Examining numerous water vapor absorption spectra of solar radiation, Gates and Harrop (1963) stated that the natural logarithm of the sun-photometric ratio is linearly related to the square root of C_w for all the strong near-IR water vapor bands. On this basis, Volz (1974) adopted a square root dependence form to derive W from the sun photometer measurements of direct solar irradiance $J(\lambda)$ taken simultaneously within two narrow passband channels, defined by means of a pair of interference filters with half-bandwidth (HBW) ≈ 0.035 μm and transmission curves peaked at the 0.94- and 0.88-μm wavelengths, respectively. Thus, the Volz

sun-photometric ratio $R_V = J(0.94\ \mu\text{m})/J(0.88\ \mu\text{m})$ was expressed as a function of C_w in the following form:

$$R_V = A \exp(-KC_w^n), \tag{2}$$

with $n = 0.5$, where (i) parameter A depends closely on the extraterrestrial values $J_o(0.94\ \mu\text{m})$ and $J_o(0.88\ \mu\text{m})$ of the two output signals, as they would be measured by the sun photometer outside the atmosphere; and (ii) coefficient K depends on the spectral absorption features of the $\rho\sigma\tau$ band, properly weighted by the spectral curves of filter transmission and sensor responsivity.

Further studies were developed on the analytical form of Eq. (2), by comparing the measurements of R_V with values of W derived from simultaneous radiosoundings, showing that a value of $n = 1/1.78 = 0.5618$ can be used in Eq. (2) with the same reliability as $n = 0.5$ (Pitts et al. 1977). Comparing sun-photometric measurements against microwave radiometric measurements of precipitable water, Bartels (1986) found that different values of exponent n, ranging between 0.04 and 0.8333, can be reliably used to give form to the dependence curve of the sun-photometric ratio on the water vapor content, provided that coefficient K in Eq. (2) is changed from one value of n to another. However, he suggested adopting the value of $n = 0.5$ to determine W within the range of this quantity from 2.5 to 9.6 cm, and pointed out that nothing can be said about the analytical form assumed by the dependence curve of sun-photometric ratio on C_w for very low values of W, a region where Bird and Hulstrom (1982) reported difficulty. The Antarctic atmosphere frequently presents very low values of W, which are associated with very dry air conditions. Examining a set of sun-photometric ratio measurements performed at TNB during the austral summer periods of 1988 and 1989, Tomasi et al. (1990) found average values of n decreasing from 0.927 to 0.509 throughout the overall range of C_w from 0.4 to 6.1 cm. These findings suggest that values of $n > 0.5$ can be suitably used for determining W from sun photometer measurements taken at coastal Antarctic sites. Thus, the present analysis of sun-photometric data recorded at the TNB, HN, and Dome C sites could provide a useful contribution for clarifying such aspects.

Evidence of the variability of exponent n as a function of C_w also emerges from the analysis of the atmospheric transmittance evaluations made by Eldridge (1967) in terms of error function absorption coefficients equal to 0.018 and 0.19 $\text{cm}^{-1/2}$ at the 0.85- and 0.95-μm wavelengths, respectively. Such values of monochromatic atmospheric transmittances $\tau_E(0.95\ \mu\text{m})$ and $\tau_E(0.85\ \mu\text{m})$ are presented in Fig. 1 throughout the range of C_w from 10^{-2} to 10^2 cm, showing that these transmittance functions decrease gradually with strongly different rates. The values of ratio $R_E = \tau_E(0.95\ \mu\text{m})/\tau_E(0.85\ \mu\text{m})$ are given in Fig. 1 as a function of C_w, over a bilogarithmic scale. Therefore, bearing in mind that R_E is proportional to the sun-photometric ratio, the absolute value of the slope coefficient of such a curve yields reliable evaluations of exponent n used in Eq. (2), throughout a very wide range of C_w, presenting (i) an average value of about 0.96 within the range $0.01 \leq C_w \leq 0.02$ cm, and (ii) gradually decreasing values as C_w increases by four orders of magnitude, until assuming an average value of 0.59, within the range $50 \leq C_w \leq 100$ cm. This behavior of parameter n agrees very well with that predicted by the Matheson diagram, defined for arrays of unequal but independent lines giving form to an absorption band (Goody 1964). In particular, the Eldridge (1967) calculations indicate that n is expected to present (i) gradually decreasing values as C_w increases at all the Antarctic sites, and (ii) values ranging between 0.6 and 0.8 at the high-altitude sites, where C_w is most frequently observed to vary between 0.02 and 0.4 cm, for values of $m_w < 5$.

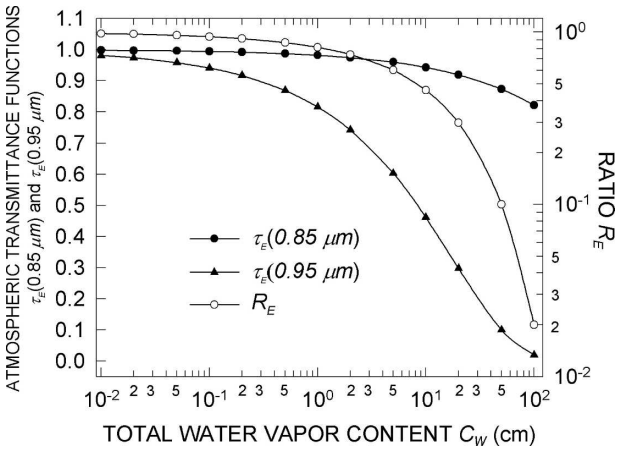

FIG. 1. Dependence curves of the atmospheric transmittance functions $\tau_E(0.95\ \mu\text{m})$ and $\tau_E(0.85\ \mu\text{m})$ (given on the left scale) on the total water vapor content C_w, as determined by Eldridge (1967). The dependence curve of ratio $R_E = \tau_E(0.95\ \mu\text{m})/\tau_E(0.85\ \mu\text{m})$ on parameter C_w is also shown, ratio R_E being defined on the right ordinate scale.

3. The field measurements of the sun-photometric ratio

The field measurements were performed by Valenziano et al. (1998) at different Antarctic sites, using simultaneously the portable Volz (1974) sun photom-

eter number 625 and one of the sun photometers number 1 and number 2. The Volz sun photometer was equipped with four passband interference filters, two of which were centered at the 0.946-μm (with HBW = 0.032 μm) and 0.868-μm (with HBW = 0.034 μm) wavelengths, respectively, to provide measurements of ratio $R_V = J(0.946\ \mu\text{m})/J(0.868\ \mu\text{m})$. The sun photometer number 1 was equipped with two interference filters having peak wavelengths of $\lambda_p = 0.9407\ \mu$m [with HBW = 0.0134 μm and peak transmittance $F(\lambda_p) = 49.2\%$] and $\lambda_p = 0.8691\ \mu$m [with HBW = 0.0112 μm, and $F(\lambda_p) = 59.0\%$]. Thus, the ratio $R_1 = V(0.9407\ \mu\text{m})/V(0.8691\ \mu\text{m})$ was determined from each pair of output voltages measured simultaneously. Sun photometer number 2 was similarly equipped with two interference filters having $\lambda_p = 0.9385\ \mu$m [HBW = 0.0122 μm, $F(\lambda_p) = 53.5\%$] and $\lambda_p = 0.8702\ \mu$m [HBW = 0.0116 μm, $F(\lambda_p) = 55.0\%$], providing the output voltages $V(0.9385\ \mu\text{m})$ and $V(0.8702\ \mu\text{m})$, respectively, from which the ratio $R_2 = V(0.9385\ \mu\text{m})/V(0.8702\ \mu\text{m})$ was determined. The direct solar irradiance measured by the two instruments within their channels was converted into output voltages by means of amplification devices with different gain factors g_i within the band and window channels (indicated by subscripts $i = 1$ and $i = 2$, respectively) to obtain comparable signals within the two channels. In fact, the band-channel irradiance measurements are in general considerably lower than those measured in the windows for all the SZA values, because of water vapor absorption. Thus, the band signals were amplified to a greater extent than the window ones, with an amplification ratio $G = g_1/g_2$ equal to 5.70 in both sun photometers number 1 and number 2.

The two instruments were pointed at the sun by means of a collimating optical device with an angular precision better than 0.2°. The optical system used to measure the direct solar irradiance consisted of (i) an entrance circular diaphragm of 5-mm diameter, combined with two supplementary circular diaphragms to limit a field-of-view of about 1.5°-diameter, (ii) a rotating wheel with two circular holes containing the two interference filters defining the band and window channels, and (iii) an UDT-450 Photop used as sensor. By means of a switch, the two interference filters were consecutively placed on the optical axis within a few seconds, connected with the different amplification devices mentioned above, to furnish the output signals.

The field measurements of sun-photometric ratios R_1 and R_2 were performed at three sites, collecting the following five sets of measurements:

1) Dataset OASI-A, consisting of measurements of R_1 and W, taken at the Osservatorio Antartico Submillimetrico e Infrarosso (OASI) astronomical site, located on the summit of a rocky hill (92 m MSL) facing the TNB Mario Zucchelli Italian station on the Ross Sea coast. The measurements were performed during the period from 29 October to 13 November 1993, using the sun photometers number 1 and number 625.
2) Dataset OASI-B, consisting of measurements of R_1 and W, taken at the OASI site, during the period from 30 October to 21 November 1994, employing the same instruments as for set OASI-A.
3) Dataset OASI-C, consisting of measurements of R_2 and W, taken at the OASI site, during the period from 11 to 18 December 1996, with sun photometers number 2 and number 625.
4) Dataset HN, consisting of measurements of R_1 and W, taken at the HN high-altitude site in Northern Victoria Land, about 200 km NW of OASI, during the period from 23 November to 20 December 1994, with sun photometers number 1 and number 625.
5) Dataset Dome C, consisting of simultaneous measurements of R_2 and W, taken at the Dome C Observatory over the Antarctic Plateau, during the period from 28 December 1996 to 12 January 1997, using sun photometer number 2 only.

The reliability of the two sun photometers in measuring the direct solar irradiance within the two spectral channels was tested through comparisons between the output voltages provided simultaneously by the two sun photometers and the Volz sun photometer at the OASI and HN sites, as shown in Fig. 2. The tests indicate that the output voltages of the two present sun photometers are proportional with a good approximation to those of sun photometer number 625 in both channels, with a standard error of estimate $\sigma_{y,x}$ equal to 0.04 for the window channels and 0.11 for the band channels. The dispersion of data, evaluated within ±10% on the average, is mainly due to the filter transmission variations occurring from one measurement period to another, as can be noticed in Fig. 2, and to a lesser extent (by 3%–7%) it is due to the instrumental errors. For instance, the band signals of the OASI-B set appear to be subject to an appreciable decrease in 1994, by percentages varying between 9% and 25% with respect to the same band signals measured in the previous campaign of 1993, while other less marked variations in the window filter transmission appear evident in Fig. 2, from one campaign to another. These variations indicate that aging effects on the filter took place, causing a sharp decrease in the peak transmission at the 0.9407-μm wavelength, from 49.2% to less than 40%, and more limited variations, not exceeding 7%, in the window-

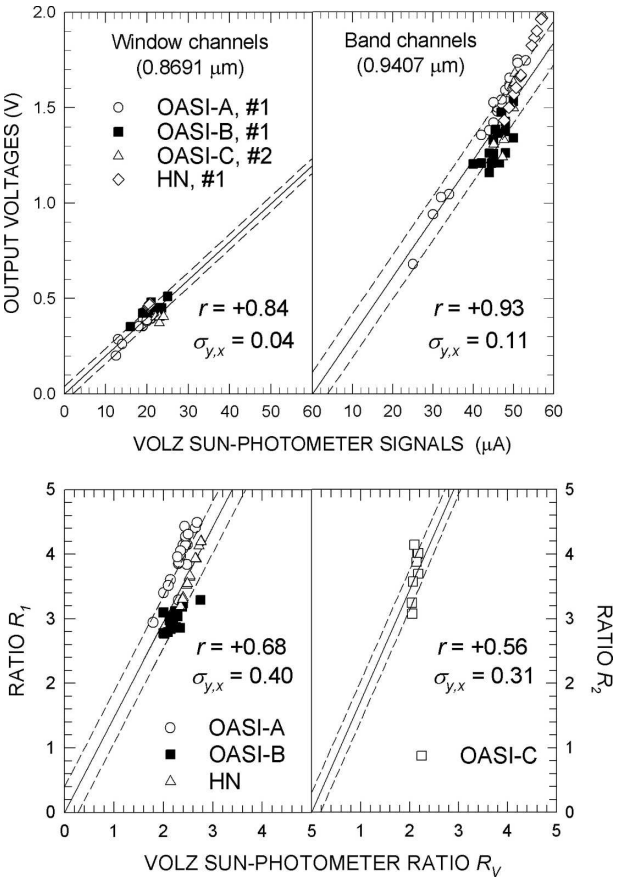

FIG. 2. (top left) Comparison between the output voltages provided by the two sun photometers number 1 and number 2 within the window channels, and the simultaneous signals measured with the Volz sun photometer number 625 within the 0.868-μm channel, during the OASI-A, OASI-B, OASI-C, and HN campaigns. (top right) As on the left, for the output voltages provided by the same instruments within the water vapor band channels. The solid lines are the overall best-fit regression lines drawn through the origin, found for the values of regression coefficient r given in the graphs. The dashed lines are drawn parallel to the regression lines for standard errors of estimate $\sigma_{y,x}$ equal to 0.04 (top left) and 0.11 (top right). The measurement errors were evaluated to range between 2% and 5% and were not shown in the graph since the corresponding bars are smaller than the symbol sizes. (bottom left) Comparison between the sun-photometric ratio R_1, measured by the sun photometer number 1 during the OASI-A, OASI-B, and HN campaigns, and the simultaneous measurements of ratio R_V obtained with the Volz sun photometer number 625. (bottom right) As in (left), for the values of sun-photometric ratio R_2 measured during the OASI-C campaign with the sun photometer number 2, and the simultaneous measurements of ratio R_V taken with the Volz sun photometer number 625. The solid lines are the overall best-fit regression lines drawn through the origin, found for the values of regression coefficient r given in the graphs. The dashed lines are drawn parallel to the regression lines for standard errors of estimate $\sigma_{y,x}$ equal to 0.40 (bottom left) and 0.31 (bottom right). The measurement errors were evaluated to vary between 4% and 7%.

channel transmission. The variations were found to be consistent with the transmission decrease of more than 20% found for the band filter of sun photometer number 1 during the laboratory tests performed after the Antarctic campaign, in 1997, and with the transmission decreases of 3%–7% tested for the window filters of both instruments, during the final laboratory check. The comparison between the pairs of ratios (R_1, R_V) and (R_2, R_V), shown in the lower part of Fig. 2, confirms that the values of R_1 taken at the OASI site in 1994 were subject to an appreciable lowering with respect to 1993, while those measured from 1994 to 1996 appear to be less important. This comparison also shows that sun photometer number 2 has greater sensitivity than sun photometer number 625.

The laboratory spectral curves of filter transmission $F(\lambda)$ measured before the 1993 campaign are shown in Fig. 3 for both instruments, throughout the wavelength range from 0.80 to 1.00 μm, together with the spectral responsivity curve $\rho(\lambda)$ of the UDT-450 Photop sensor, as measured in 1992, before the field campaigns in Antarctica. Figure 3 also shows the spectral curve of extraterrestrial solar irradiance $I_o(\lambda)$ determined by Gueymard (2004) within the same wavelength range, for a spectral resolution $\Delta\lambda = 10^{-3}$ μm, and compares it with those of Iqbal (1983) for $\Delta\lambda = 10^{-2}$ μm, and of Neckel and Labs (1984) for $\Delta\lambda = 2 \times 10^{-3}$ μm, indicating very clearly that the Gueymard (2004) data are the most suitable for use in the present study.

4. Spectral transmittance features of five Antarctic atmosphere models

Figure 2 gives evidence of the marked changes in the sun photometer responsivity occurring from one field campaign to another, as well as of the large scatter of the signals due to instrumental errors. Thus, an empirical calibration of the sun photometer ratios based only on field measurements could define shape parameters of the calibration curves influenced appreciably by the experimental scatter of data. For these reasons, it was decided to calculate the spectral curves of atmospheric transmittance, as they would be measured by the two sun photometers within their band and window channels at the OASI, HN, and Dome C sites, for the different meteorological conditions observed at the various sites. In detail, a complex procedure was adopted to determine the dependence features of ratios R_1 and R_2 on C_w, consisting of the following steps:

1) Define five Antarctic atmosphere models, for which the corresponding spectral curves of atmospheric transmittance can be calculated in the near-IR range, as done below in this section.

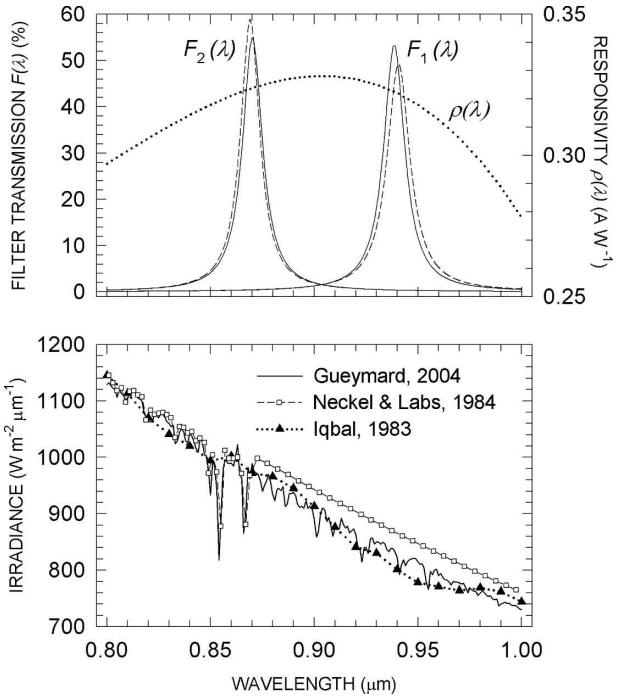

FIG. 3. (top) Spectral curves of filter transmission $F(\lambda)$ relative to the band (on the right, with subscript 1) and window filters (on the left, with subscript 2) mounted on the portable sun photometers number 1 (dashed curves) and number 2 (solid curves), compared with the spectral curve of relative responsivity $\rho(\lambda)$ of the UDT-450 Photop sensor mounted on both the two-channel sun photometers (dotted curve), throughout the 0.80–1.00-μm wavelength range. (bottom) Spectral curve of extraterrestrial solar irradiance $I_o(\lambda)$ (solid curve) determined by Gueymard (2004), used in the present study to calculate the atmospheric transmittance terms for simulating the sun photometer output signals. The extraterrestrial solar irradiance values given by Iqbal (1983) (solid triangles) and Neckel and Labs (1984) (open squares) are also shown for comparison.

2) Simulate the sun photometer signals for different values of parameters W and SZA (and, hence, relative optical air mass m_w), as done in the last part of this section.
3) Calculate the ratios between simulated values of the output signals and determine the calibration curves by plotting the ratios versus C_w, as described in section 5.
4) Define the best-fit values of the intercept constant of the calibration curves, through comparison with the field measurements of sun-photometric ratios, to account for the filter transmission changes occurring during the field campaigns, as done in section 6.

The first step of the above procedure determined the average vertical profiles of the main thermodynamic parameters (pressure, temperature, relative humidity) observed in the clear-sky Antarctic atmosphere at the three measurement sites during the field campaigns. The atmosphere models relative to the first two sites were defined using the mean vertical profiles of pressure, temperature, and dewpoint obtained by Tomasi et al. (2004) over various 10-day periods, analyzing a 12-yr set consisting of 1330 radiosoundings taken at the TNB station. Examining these datasets, Tomasi et al. (2004) found mean 10-day vertical profiles of absolute humidity with standard deviations of no more than 3% at all the tropospheric levels, giving corresponding mean 10-day values of W with standard deviations not exceeding 3%. Comparing the results obtained for the various 10-day periods, a more than threefold increase was observed in the moisture parameters (i.e., absolute humidity at tropospheric levels and precipitable water) from late October to early December, while more stable values were found during the rest of the austral summer. The dewpoint profiles were completed in the low stratosphere examining a large set of mixing ratio measurements derived from satellite data taken in high-latitude austral areas, at altitudes ranging between 10 and 30 km (Rosen et al. 1991; Rind et al. 1993; Harries et al. 1996; Lahoz et al. 1996; Chiou et al. 1997; Randel et al. 2001). Through very simple smoothing procedures, five atmosphere models were determined to describe the average meteorological conditions observed at the OASI, HN and Dome C sites during the five measurement periods defined in the previous section, as follows:

1) Model OASI-A (W = 0.127 cm), derived over the 0.092–32.000-km height range by averaging the Tomasi et al. (2004) data relative to the last 10-day period of October and the first 10-day period of November, and used to analyze the OASI-A dataset.
2) Model OASI-B (W = 0.173 cm), derived over the above height range from the data of Tomasi et al. (2004) relative to the first two 10-day periods of November, and used for analyzing the OASI-B dataset.
3) Model OASI-C (W = 0.330 cm), defined over the same height range according to the second 10-day December model of Tomasi et al. (2004), and used for the OASI-C dataset.
4) Model HN (W = 0.057 cm), determined over the 2.96–32.00-km height range by averaging the Tomasi et al. (2004) data relative to the third 10-day period of November and the first two 10-day periods of December, suitable for analyzing the HN dataset.
5) Model Dome C (W = 0.078 cm), defined using the monthly-mean vertical profiles of pressure, temperature, and humidity derived by Tomasi et al.

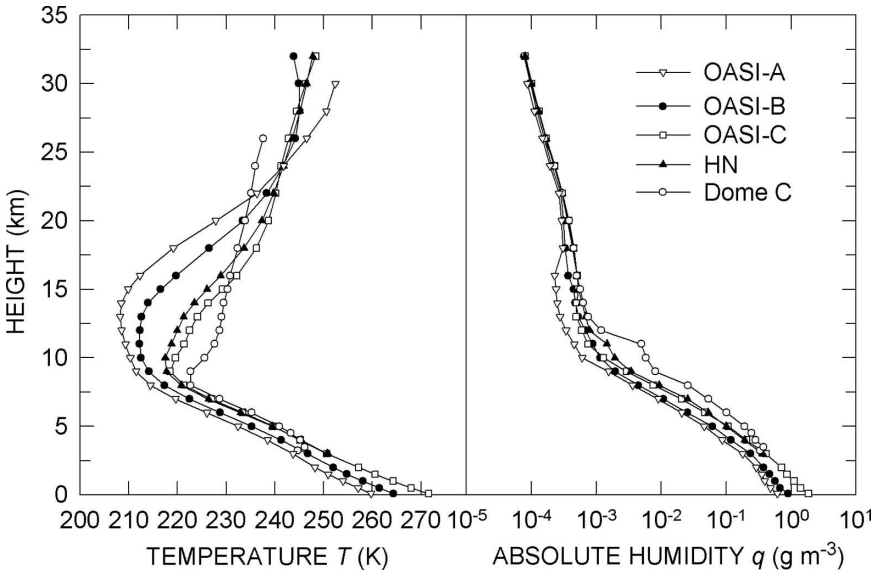

FIG. 4. Vertical profiles of air temperature $T(z)$ and absolute humidity $q(z)$ determined for the five atmosphere models OASI-A, OASI-B, OASI-C, HN, and Dome C, used to represent the average meteorological conditions of the Antarctic atmosphere during the measurement periods of the OASI-A, OASI-B, OASI-C, HN, and Dome C datasets, respectively.

(2006) through the analysis of a set of 87 radiosounding measurements performed at Dome C in January 2003 and 2004, with different Vaisala radiosonde models (Aristidi et al. 2005). This model was completed with the stratospheric vertical profiles of moisture parameters determined by Tomasi et al. (2004) for the first 10-day period of January, to cover the overall 3.25–26.00-km height range, relative to the Dome C dataset.

For the five atmosphere models, the vertical profiles of air pressure $p(z)$, temperature $T(z)$, dewpoint $T_d(z)$, relative humidity $f(z)$, and absolute humidity $q(z)$ were calculated from the surface level up to altitudes ranging between 26 and 32 km. Those of $T(z)$ and $q(z)$ are presented in Fig. 4, clearly showing that very similar values of the temperature vertical gradient were found in the tropospheric region, where a gradual warming took place from early November to mid-January. Figure 4 shows also that stratospheric temperature gradually increased from 8–10- to 25-km height during the austral summer, while the tropopause minimum decreased from more than 12- to around 8-km height. Correspondingly, the moisture conditions of the troposphere were found to increase, presenting the highest values of absolute humidity in January. All five models were completed with the vertical concentration curves of minor gases defined in the subarctic summer atmosphere model (Anderson et al. 1986) and by linking the vertical profiles of $p(z)$, $T(z)$, $T_d(z)$, and $q(z)$ with those of the subarctic summer atmosphere model from 35- to 118-km height, through linear interpolation of $T(z)$ and $T_d(z)$ and exponential interpolation of $p(z)$ and $q(z)$ in height.

In the second step of the simulation procedure, the spectral curves of atmospheric transmittance were calculated for the five atmosphere models, within the channels of the two sun photometers number 1 and number 2, using the moderate resolution atmospheric transmission MODTRAN4 code (Anderson et al. 2000), in which the water vapor selective absorption is represented with a spectral resolution of 1 nm by means of the Curtis–Godson approximation (Curtis 1952; Godson 1955). Aerosol extinction was represented in all five models assuming a visual range of 46 km for a columnar aerosol loading consisting predominantly of maritime particles, the choice being made considering that this aerosol composition was observed most frequently at TNB, in the absence of katabatic winds (Di Carmine et al. 2005). An overall number of 125 spectral curves of atmospheric transmittance were determined with the MODTRAN4 code for (i) five sets of atmospheric models, relative to the OASI-A, OASI-B, OASI-C, HN, and Dome C models, respectively, each set consisting of five submodels in which different values of relative humidity $f(z)$ were assumed at all altitudes, as obtained by multiplying those of the original models by factors equal to 0.25, 0.50, 0.75, 1.00, and 1.25, respectively, thus achieving five different values of

TABLE 1. Shape parameters of the best-fit curves found in terms of Eqs. (3)–(5) within various intervals of total water vapor content C_w, chosen for the five datasets of atmosphere configurations and the two near-IR sun photometers number 1 and number 2 used during the OASI, HN, and Dome C campaigns, together with the range of exponent n found for each interval of C_w.

Dataset	Measurement period	Sun photometer	Range of total water vapor content C_w (cm)	Intercept constant A	Polynomial coefficients in Eq. (5)			Range of exponent n
					a_1	a_2	a_3	
OASI-A	29 Oct–13 Nov 1993	1	0.05–0.65	0.843	1.069	−1.463	0.915	0.83–0.57
OASI-B	30 Oct–21 Nov 1994	1	0.07–0.90	0.833	0.923	−0.933	0.432	0.82–0.58
OASI-C	11–18 Dec 1996	2	0.13–1.70	0.834	0.704	−0.377	0.092	0.80–0.54
HN	23 Nov–20 Dec 1994	1	0.02–0.29	0.852	1.389	−4.092	5.556	0.83–0.63
Dome C	28 Dec 1996–12 Jan 1997	2	0.03–0.40	0.876	1.274	−2.758	2.828	0.83–0.61

W; and (ii) five values of the solar zenith angle SZA = 50°, 60°, 68°, 72°, and 76° for each of the 5 submodels, thus covering the solar elevation range most frequently observed during the field measurements, for values of m_w = 1.555, 1.999, 2.666, 3.229, and 4.118, respectively, as used in Eq. (1) with the Kasten (1966) formula.

Correspondingly, different intervals of C_w were found for the five atmosphere models, as given in Table 1, yielding an overall range of C_w from 0.05 to 1.70 cm at the OASI site and an overall range from 0.02 to 0.40 cm at the high-altitude HN and Dome C sites. Through these calculations of atmospheric transmittance, performed for the above 125 configurations of the Antarctic atmosphere, the corresponding spectral curves of simulated atmospheric transmittance $\tau_s(\lambda)$ were determined in the 0.80–1.00-μm wavelength range. Six examples of the curves are presented in Fig. 5:

1) Three of them are presented in the upper part of Fig. 5, being calculated for the three OASI atmosphere models and SZA = 50° (i.e., for m_w = 1.555), for three different values of W: the results show very clearly that the rough doubling of W does not cause a change in the transmittance $\tau_s(\lambda)$ within the window channels, but leads instead to a marked decrease in $\tau_s(\lambda)$ at the wavelengths occupied by the absorption lines of the water vapor band.
2) Those presented in the lower part of Fig. 5 are calculated for the Dome C model (W = 0.078 cm) and different values of SZA, showing that $\tau_s(\lambda)$ in the window channel decreases gradually as SZA increases, while $\tau_s(\lambda)$ in the absorption band channel decreases more rapidly as SZA decreases and C_w increases consequently from 0.12 to 0.25 cm.

For (i) the 125 spectral curves of $\tau_s(\lambda)$ calculated above, (ii) the spectral curves of $F_1(\lambda)$, $F_2(\lambda)$ and $\rho(\lambda)$ given in Fig. 3 for the two near-IR sun photometers, and (iii) the spectral curves of extraterrestrial solar irradiance $I_o(\lambda)$ in Fig. 3, the simulated output signals $J_s(\lambda_i)$ were calculated within the band and window channels in terms of the following equation:

$$J_s(\lambda_i) = g_i \int_{\lambda_a}^{\lambda_b} I_o(\lambda)\tau_s(\lambda)F_i(\lambda)\rho(\lambda)\, d\lambda, \qquad (3)$$

where λ_i is the peak wavelength of one of the two spectral channels (labeled with subscript i = 1 for the band channel and i = 2 for the window channel), and λ_a and λ_b are the limits of the integration spectral range relative to the spectral channel under consideration. Some examples of spectral curves of the function $I_o(\lambda)$ $\tau_s(\lambda)$ $F_i(\lambda)$ $\rho(\lambda)$ under integration in Eq. (3) are shown in Fig. 6, together with the corresponding curves of $\tau_s(\lambda)$ over the 0.80–1.00-μm wavelength range. Following this procedure, the pairs of simulated signals $J_s(\lambda_i)$ were determined for all the 125 atmospheric configurations, from which the corresponding values of simulated sun-photometric ratios $R_{s1} = J_s(0.9407\ \mu\text{m})/J_s(0.8691\ \mu\text{m})$ and $R_{s2} = J_s(0.9385\ \mu\text{m})/J_s(0.8702\ \mu\text{m})$ were obtained for the two sun photometers number 1 and number 2.

5. Definition of the simulated calibration curves of sun-photometric ratio

The third step of the present procedure included the calculations of simulated ratios R_{s1} and R_{s2}, relative to the two near-IR sun photometers number 1 and number 2, respectively. The overall set of 125 values of ratios R_{s1} and R_{s2} were plotted versus the total water vapor content C_w in Fig. 7, separately for the five subsets pertaining to the atmosphere models OASI-A, OASI-B, OASI-C, HN, and Dome C. Each subset consists of 25 sun-photometric ratios relative to values of C_w increasing in regular steps throughout the corresponding interval of C_w given in Table 1. The comparison between the simulated curves OASI-A and OASI-B in Fig. 7 shows that ratio R_{s1} depends very

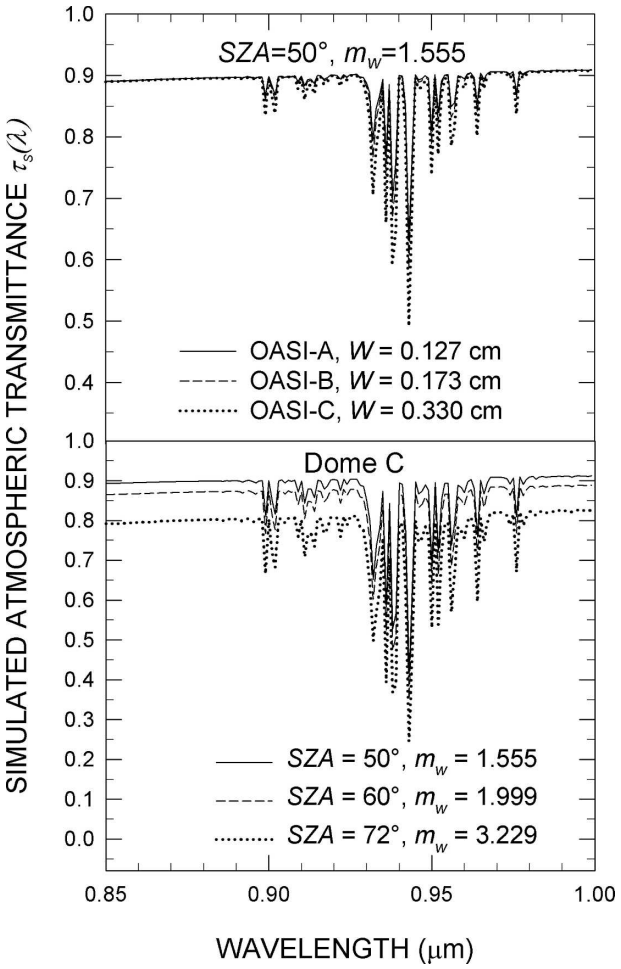

FIG. 5. (top) Spectral curves of simulated atmospheric transmittance $\tau_s(\lambda)$, calculated to evaluate the sun-photometric ratio R_{s1}, in three simulation cases relative to the three OASI atmosphere models, for the same values of solar zenith angle SZA and relative optical air mass m_w. (bottom) As in (top), for evaluating the sun-photometric ratio R_{s2} of sun photometer number 2, in three simulation cases relative to the Dome C atmosphere model for different pairs of parameters SZA and m_w.

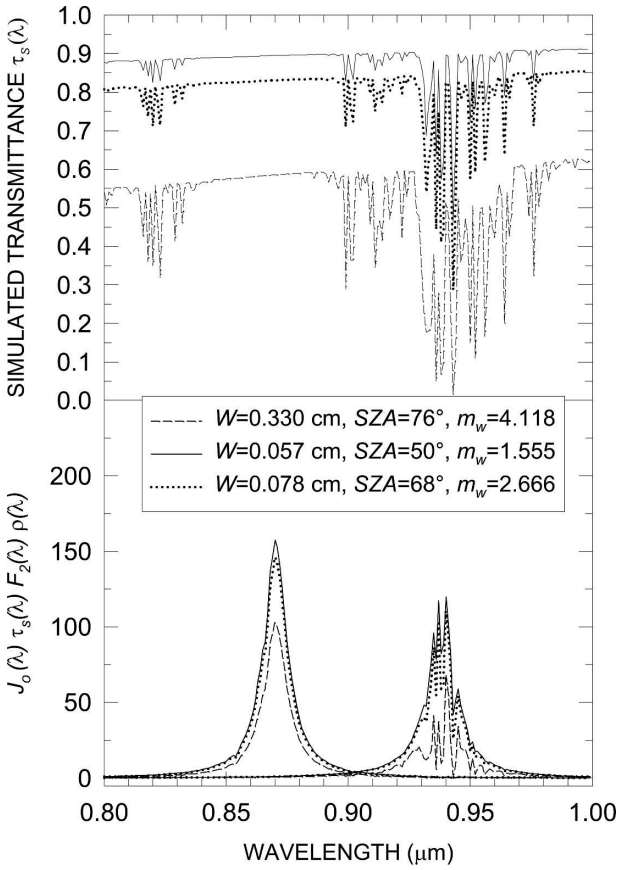

FIG. 6. (top) Spectral curves of simulated atmospheric transmittance $\tau_s(\lambda)$, calculated for three atmospheric simulation cases relative to (i) model OASI-C with W = 0.330 cm, SZA = 76°, and m_w = 4.118; (ii) model HN with W = 0.057 cm, SZA = 50°, and m_w = 1.555; and (iii) model Dome C with W = 0.078 cm, SZA = 68°, and m_w = 2.666. (bottom) Corresponding curves of the function $I_o(\lambda)\ \tau_s(\lambda)\ F_2(\lambda)\ \rho(\lambda)$ under integration in Eq. (3), relative to sun photometer number 2 and determined using the spectral curves of $I_o(\lambda)$, $F_2(\lambda)$, and $\rho(\lambda)$ given in Fig. 3, together with the curves of $\tau_s(\lambda)$ shown in (top).

weakly on the vertical profile of absolute humidity considered in the simulations. It presents discrepancies of less than 0.3% throughout the entire range of C_w, although the vertical distribution curves of $q(z)$ relative to the OASI-A and -B atmosphere models exhibit differences of 25%–30% at the low-tropospheric levels, and nearly 20% in the upper troposphere (see Fig. 4). As can be seen, the values of ratios R_{s1} and R_{s2} decrease gradually with C_w, and each set can be easily fitted by a polynomial curve. According to Eq. (2), and bearing in mind the above remarks on the variability of exponent n, the simulated ratios R_{s1} and R_{s2} are expected to vary as a function of C_w following the general analytical form

$$R_s = A \exp[-f(C_w)], \tag{4}$$

where (i) the intercept constant A accounts for the variations due to the extraterrestrial solar spectrum, and the amplification gain G evaluated in section 3, and (ii) the function $f(C_w)$ can be represented by means of a polynomial curve, as shown in Fig. 7. Thus, the simulated values of ratios R_{s1} and R_{s2} calculated above were best fitted by three-term polynomial curves having the general form

$$f(C_w) = a_1 C_w + a_2 C_w^2 + a_3 C_w^3, \tag{5}$$

where the shape parameters can be defined separately for each of the five datasets of ratios R_{s1} and R_{s2}, within the corresponding interval of C_w given in Table 1. The

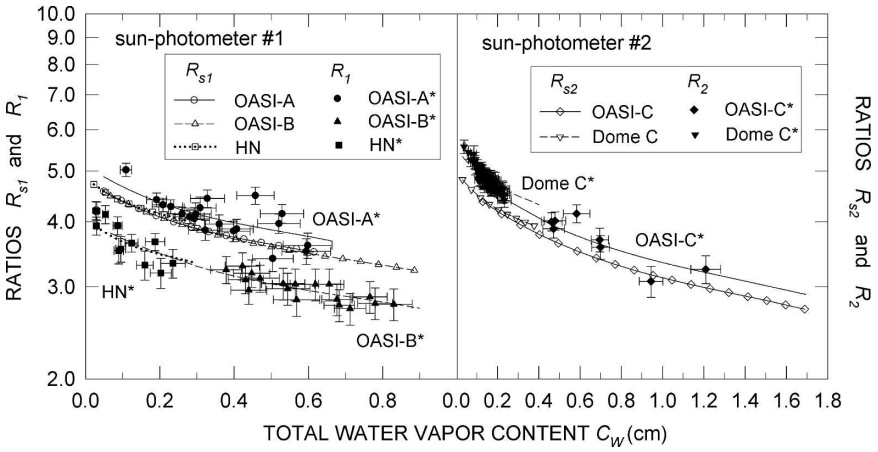

FIG. 7. (left) Comparison between the simulated values of ratio R_{s1} (open symbols) plotted vs total water vapor content C_w, as obtained for the models OASI-A, OASI-B, and HN, respectively, and the measured values of sun-photometric ratio R_1 (solid symbols) plotted vs C_w. The simulated curves were then shifted upward (OASI-A) or downward (OASI-B and HN) to obtain the best fit of the curves with the field data, and hence evaluate the relative correction factors Δ for the corresponding calibration curves OASI-A*, OASI-B*, and HN*, suitable for analyzing the field measurements. (right) As in (left), for simulated ratios R_{s2} and measured ratios R_2 of the sun photometer number 2, relative to the OASI-C and Dome C models, providing the simulated calibration curves OASI-C and Dome C together with the field calibration curves OASI-C* and Dome C* for the relative correction factors Δ suitable for the field measurements taken at the high-altitude Antarctic sites. The vertical and horizontal bars give the measurement errors.

best-fit curves, labeled OASI-A, OASI-B, OASI-C, HN, and Dome C in Fig. 7, were thus determined for the values of intercept constant A and polynomial coefficients a_1, a_2, and a_3 given in Table 1. It can be noticed that the discrepancies between the values of A were found to be within about $\pm 1\%$ at the OASI and HN sites, while an increase of about 5% was found passing from the OASI-C to the Dome C dataset. All the five best-fit calibration curves decrease as a function of C_w with values of the slope coefficient n in Eq. (2) given by the derivative $d \ln f(C_w)/d \ln C_w$, which were found to decrease gradually from 0.83 to 0.54 at the sea level Antarctic sites, and from 0.83 to 0.61 at the high-altitude sites of the Antarctic Plateau, as can be seen in Table 1. Such results were obtained over the range $0.02 \leq W \leq 0.55$ cm at the OASI coastal site and the overall range $0.01 \leq W \leq 0.13$ cm at the HN and Dome C high-altitude sites, which both differ considerably from the $2.5 \leq W \leq 9.6$-cm range examined by Bartels (1986). Therefore, the present results can be more realistically compared with the variable features of parameter n shown in Fig. 1 as a function of total content C_w (over the Antarctic range $C_w < 1.5$ cm), as derived from the Eldridge (1967) calculations, rather than with the Bartels (1986) results obtained for a different range of precipitable water.

6. Correction of the intercept constant

The fourth step of the present calibration procedure consists of the correction of the values of intercept constant A of the simulated curves, through comparison with the field measurements of the sun-photometric ratios and water vapor content C_w. This quantity was calculated according to Eq. (1), for (i) values of m_w determined for each sun-photometric ratio in terms of the Kasten (1966) formula given as a function of the apparent SZA, which varies with latitude, longitude, and UT measurement time; (ii) values of W determined for each sun-photometric ratio of the OASI-A, OASI-B, and OASI-C datasets, following the so-called precipitable water interpolation in time (PWIT) procedure described in the appendix, which utilizes local meteorological and radiosounding measurements; and (iii) values of W, relative to the HN and Dome C datasets, measured directly by Valenziano et al. (1998), since simultaneous radiosounding and ground-level meteorological data were not available at these high-altitude sites in 1996.

Figure 7 shows the field measurements of ratios R_1 and R_2, which are affected by instrumental errors estimated in Fig. 2 to vary between 3% and 7%. Since the corrections for dry bias and lag errors applied to the

radiosounding data following the Tomasi et al. (2006) procedure lead to supplemental errors of a few percents in evaluating W, it can be stated that the overall error of C_w is given by the sum of (i) the error arising directly from the analysis of the radiosounding data, realistically evaluated to vary between 5% and 10% on average; (ii) the error due to the use of the PWIT interpolation procedure, evaluated in the appendix to range usually between 2% and 4%; and (iii) the error due to the dry bias corrections, which are relatively small, as mentioned above. The data are shown in Fig. 7 with their error bars evaluated according to the above estimates. The comparison made in the left part of Fig. 7 regards the measurements of R_1 taken by sun photometer number 1 during the OASI-A, OASI-B, and HN campaigns. It shows that the simulated values of R_{s1} fall between the OASI-A sequence of R_1 measured in 1993 and the OASI-B and HN series of R_1 recorded in 1994 and 1996, respectively. The results relative to sun photometer number 2 are presented in the right part of Fig. 7, showing that the simulated values of R_{s2} are appreciably lower than those of R_2 measured during the OASI-C and Dome C campaigns. These differences can be plausibly explained as due to variations in the filter transmission characteristics of the sun photometers evidenced in Fig. 2. Thus, to obtain the best fit of the simulated curves of R_{s1} and R_{s2} with the experimental data, the variations in the intercept constant A caused by filter transmission changes were taken into account by multiplying the values of A given in Table 1 for the five atmosphere models by a correction factor Δ. This correction term was determined in Fig. 7 by shifting the simulated calibration curves upward or downward, until fitting the corresponding experimental data. Considering that the filter transmission can only decrease because of aging effects (sometimes, associated with slight peak wavelength shifts), factor Δ may become lower than unity in cases where the band-channel transmission decreases, and higher than unity in cases where the window-channel transmission decreases with age.

The correction factor Δ was thus determined for each curve, obtaining the best fit of the calibration curve with the field measurements. Through this procedure, new calibration curves were drawn in Fig. 7, having the same shape parameters of the simulated curves but new values of the intercept constant, modified to take into account the changes occurring in the filter transmission characteristics of the two-channel sun photometers. These curves are shown in Fig. 7, labeled as OASI-A*, OASI-B*, OASI-C*, HN*, and Dome C*, respectively, to distinguish them from the corresponding simulated curves OASI-A, OASI-B, and HN pertaining to ratio R_{s1} and curves OASI-C and Dome C to ratio R_{s2}, presented initially in Fig. 7. The new curves were obtained for the following best-fit values of the correction factor Δ:

1) $\Delta_{\text{OASI-A*}} = 1.063 \pm 0.032$, fitting the measurements of R_1 performed at the OASI site in late October and early November 1993, over the experimental range $0.05 \leq C_w \leq 0.65$ cm.
2) $\Delta_{\text{OASI-B*}} = 0.850 \pm 0.022$, fitting the measurements of R_1 taken at the OASI site in 1994, over the measurement range $0.067 \leq C_w \leq 0.90$ cm. This correction term turns out to be lower than unity and about 20% lower than the one evaluated in 1993, and is consistent with the aging effects on the peak transmission of the band filter, plausibly occurring from 1993 to 1994.
3) $\Delta_{\text{OASI-C*}} = 1.069 \pm 0.021$, fitting the measurements of ratio R_2 taken at the OASI site in December 1996, over the field range $0.13 \leq C_w \leq 1.70$ cm.
4) $\Delta_{\text{HN*}} = 0.837 \pm 0.047$, fitting the measurements of ratio R_1 performed at the HN site in November and December 1994, over the experimental range $0.02 \leq C_w \leq 0.29$ cm, and indicating the occurrence of further slight variations in the band filter transmission.
5) $\Delta_{\text{DOME C}} = 1.107 \pm 0.030$, fitting the measurements of ratio R_2 performed by Valenziano et al. (1998) at Dome C in the austral summer of 1996/97, and found over the application range $0.03 \leq C_w \leq 0.40$ cm.

To check the reliability of the above five calibration curves defining the dependence features of sun-photometric ratio on total content C_w, the values of the standard error of estimate $\Sigma_{y,x}$ were calculated for the field data shown in Fig. 7, separately for each of the five curves, finding values of $\Sigma_{y,x}$ equal to $\pm 4\%$ (OASI-A* and OASI-B*), $\pm 3\%$ (OASI-C* and Dome C*), and $\pm 7\%$ (HN*). The right part of Fig. 7 presents the Dome C* calibration curve, comparing it with the field data, which are apparently in poor agreement, because of their "wide" dispersion. Such features are due to the fact that sun photometer number 2 recorded part of the absorption band-channel signals close or slightly beyond the full scale of the instrument. The latter cases were labeled "upper limit" (UL) by Valenziano et al. (1998). The occurrence of the UL cases implied that the corresponding sun-photometric ratios R_2 measured at Dome C were underestimated by a few percents. Nevertheless, the standard error of estimate was found to be equal to $\pm 3\%$ for the overall set of Dome C mea-

surements, showing that the dispersion of such field data was really rather limited.

7. Determination of the precipitable water time patterns

The above values of Δ were found to vary appreciably from one dataset to another, for both sun photometers, because of the different interference filter aging. The variations in Δ determined in Fig. 7 are appreciably larger than those found for the intercept constant A in Table 1. They are presumably due to the filter degradation occurring over the 3-yr observation period, which was characterized by very harsh environment conditions in Antarctica. Using the calibration curves labeled OASI-A*, OASI-B*, OASI-C*, HN*, and Dome C* in Fig. 7, the various field datasets of ratios R_1 or R_2 were analyzed to determine the time patterns of W during the various campaigns. They are compared in Fig. 8 with those derived from the analysis of the same measurements of R_1 or R_2 applied to the square root calibration curves used by Valenziano et al. (1998). The figure shows that the use of the present refined calibration curves yields in general values of W, which are (i) lower than the square root ones for the very dry air conditions of the atmosphere at the high-altitude sites and (ii) higher than the square root ones for the relatively more humid air conditions observed at the sea level sites.

The differences between the present values of W and those given by the square root calibration curves can be better appreciated in Fig. 9, in which the present measurements of W, relative to the five datasets OASI-A, OASI-B, OASI-C, HN, and Dome C, are plotted versus those derived from the same measurements using the square root calibration curves of Valenziano et al. (1998). The comparison relative to the high-altitude HN and Dome C datasets shows that the present values of W, compared with the square root ones, are (i) lower by 10%–40% for $W < 0.05$ cm, which contains 19% of the total dataset, (ii) comparable within ±5%, in the $0.05 \leq W \leq 0.09$-cm range, containing 67% of data, and (iii) higher by 5%–10% for $W > 0.09$ cm, including the residual 14% of data. The regression lines of the datasets OASI-A, OASI-B, and OASI-C, determined over the upper range of W from 0.1 to 0.6 cm, were all found to have negative intercept constants and slope coefficients ranging between 1.16 and 1.42, with regression coefficients higher than +0.99 in all the three cases, as shown in Table 2. The present OASI values of W turn out to be comparable with the square root ones (mainly within ±10%) for $W < 0.3$ cm, and gradually higher by 5%–15% for values of W increasing from 0.3 to 0.6 cm.

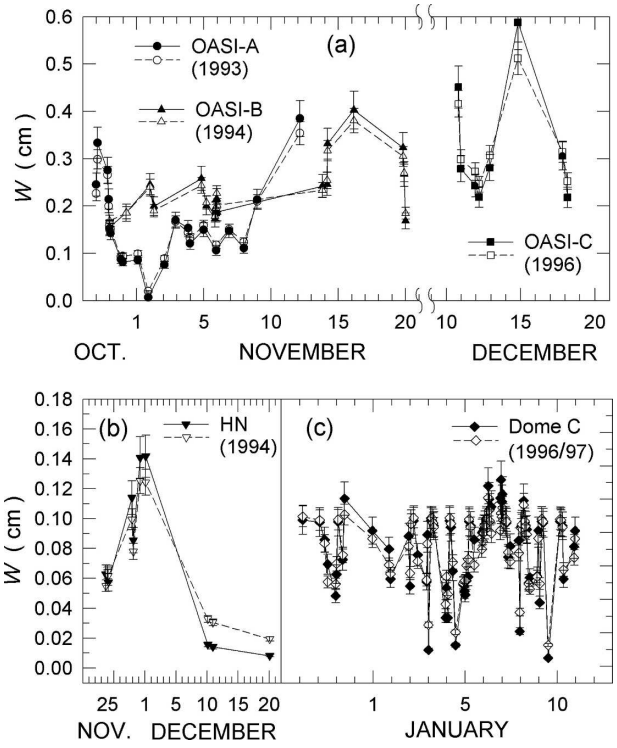

FIG. 8. (a) Time patterns of precipitable water W determined by analyzing the sets of sun-photometric ratios R_1 and R_2 measured during the OASI-A, OASI-B, and OASI-C campaigns using (i) the present calibration curves (solid symbols) and (ii) the square root calibration curves of Valenziano et al. (1998) (open symbols). (bottom) As in (a), for the sets of sun-photometric ratios R_1 and R_2 measured during the (b) HN and (c) Dome C campaigns. The vertical bars give the measurement errors.

In addition, the present estimates of W obtained for the three OASI and HN datasets are compared in Fig. 10 with those derived from the simultaneous measurements performed with the Volz sun photometer number 625 and analyzed with its square root calibration curve. The results are given in Fig. 10 with their errors, represented by vertical and horizontal bars and found to vary mainly between ±4% and ±10%. These data appear to be more dispersed than those in Fig. 9, as confirmed by the lower values of the regression coefficients determined in Table 2 for the three OASI datasets, evaluated to vary between +0.83 and +0.94 against those determined in the test of Fig. 9, all exceeding +0.99. Obtained at the OASI coastal site, such results could be due to the worse performances of the Volz sun photometer compared to the sun photometers number 1 and number 2. Conversely, very close values of the regression coefficient were found at the HN site in both tests, suggesting that the Volz sun photometer and sun photometers number 1 and number 2 had simi-

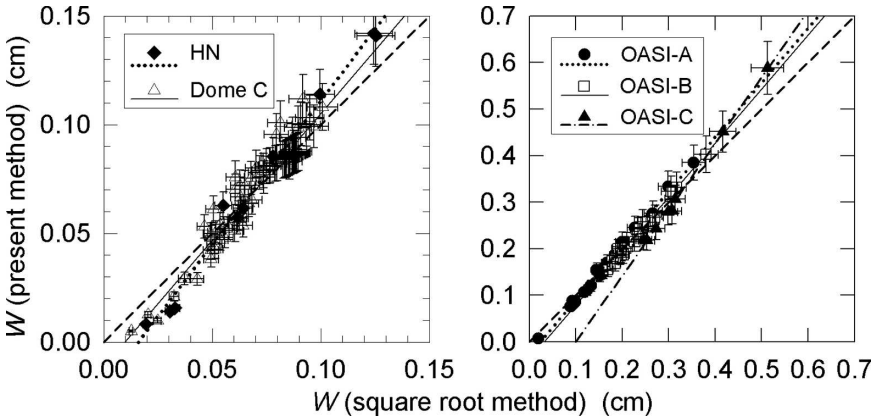

FIG. 9. (left) Comparison test made by plotting the present measurements of precipitable water W obtained from the sets of sun-photometric ratios measured during the HN and Dome C field campaigns (using the HN* and Dome C* calibration curves, respectively) vs the values of W obtained from the same sets using the square root calibration curves determined by Valenziano et al. (1998). (right) As in (left), for the measurements of W obtained from the sets of sun-photometric ratios measured during the three OASI field campaigns. In both (right) and (left), the vertical and horizontal bars give the measurement errors, varying mainly between ±4% and ±10%. The regression lines are drawn for comparison with the bisecting (dashed) line. The values of intercept constant w_o and slope coefficient χ_w of the five regression lines are given in Table 2, together with their regression coefficients.

lar performances at the high-altitude HN site, being unable to provide measurements of the atmospheric water vapor absorption with the same precision as at the coastal sites.

TABLE 2. Values of intercept w_o, slope coefficient χ_w, and regression coefficient r of the regression lines obtained through the comparison tests shown in Figs. 9 and 10. The tests of Fig. 9 were made by comparing (i) the values of precipitable water W obtained from the sets OASI-A, OASI-B, OASI-C, HN, and Dome C of measurements taken with sun photometers number 1 and number 2, using the present calibration curves and (ii) those obtained from the same measurements, using the square root calibration curves determined by Valenziano et al. (1998). The comparison test shown in Fig. 10 was made for (i) the values of W obtained from the sets OASI-A, OASI-B, OASI-C, and HN of measurements given by sun photometers number 1 and number 2, using the present calibration curves, and (ii) those obtained from the Volz sun photometer number 625 measurements, using its square root calibration curve.

Dataset	Intercept w_o (cm)	Slope coefficient χ_w	Regression coefficient r
	Test in Fig. 9		
OASI-A	−0.027	1.170	+0.997
OASI-B	−0.038	1.163	+0.992
OASI-C	−0.142	1.421	+0.998
HN	−0.021	1.321	+0.994
Dome C	−0.011	1.165	+0.963
	Comparison in Fig. 10		
OASI-A	0.018	0.838	+0.939
OASI-B	0.078	0.684	+0.833
OASI-C	0.019	0.896	+0.894
HN	−0.021	1.343	+0.995

8. Conclusions

The present results demonstrate that multichannel sun photometers, manufactured with narrowband interference filters with HBW < 0.01 μm, can be employed at both coastal and Antarctic Plateau sites, using calibration curves of the sun-photometric ratios characterized by relatively low values of the standard error of estimate $\Sigma_{y,x}$, provided that polynomial calibration curves are used, like those defined in the present study. For the present calibration curves, the values of $\Sigma_{y,x}$ were found to be within ±4% at the coastal sites and within ±7% at the high-altitude sites, these refined calibration curves taking into account the variability of the absorption intensity as a function of the water vapor amount along the sun path, at various altitudes. As shown in Fig. 10, the results provide better estimates of W than those determined by Valenziano et al. (1998) using a procedure based on the Volz (1974) square root absorption law. In fact, the results achieved here are based on simulations of the sun photometer output voltages made by (i) evaluating the transmittance features of the atmosphere, using models representing the particularly dry air conditions of the Antarctic atmosphere; (ii) considering realistically the spectral characteristics of extraterrestrial solar irradiance, and instrumental responsivity, and the gain factors of the amplification devices; and (iii) normalizing the ratios of the simulated signals to the field measurements of the sun-photometric ratio, in such a way as to account for the

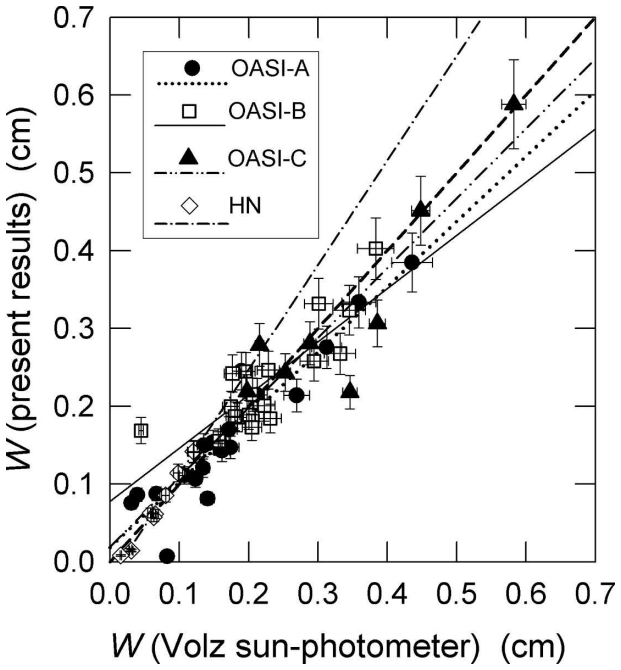

FIG. 10. Plot of the present measurements of precipitable water W obtained from sets OASI-A, OASI-B, OASI-C, and HN of sun-photometric ratios (using the calibration curves OASI-A*, OASI-B*, OASI-C*, and HN*) vs the values of W obtained from the simultaneous measurements of sun-photometric ratio taken with the Volz sun photometer number 625, and examined in terms of its square root calibration curve. The vertical and horizontal bars give the measurement errors, varying mainly between ±4% and ±10%, respectively. The regression lines were drawn to give a measure of the dispersion of data, as found for the values of intercept constant w_o and slope coefficient χ_w given in Table 2, together with their regression coefficients.

changes in the transmission characteristics of the interference filters that occur during the field campaigns, for the extremely harsh conditions of the Antarctic atmosphere.

Acknowledgments. This research was supported by the Programma Nazionale di Ricerche in Antartide (PNRA) and developed as a part of subproject 2006/6.01: POLAR-AOD: A network to characterize the means, variability and trends of the climate-forcing properties of aerosols in polar regions. The authors also thank the International Center for Theoretical Physics (ICTP, Trieste, Italy) for its support in the form of the participation of B. Petkov, in the frame of the Programme for Training and Research in Italian Laboratories.

APPENDIX

The Precipitable Water Interpolation in Time Procedure

The precipitable water interpolation in time (PWIT) procedure was adopted in order to determine more precise values of W at the measurement times than those given by the local Vaisala RS80-A radiosoundings. It utilizes the radiosonde measurements performed routinely at the TNB station twice every day, at 0000 and 1200 UTC, and takes into account the daily time patterns of absolute humidity q_o at the surface, derived from the surface data recorded routinely at the Eneide meteorological station, not far from the OASI site.

The PWIT procedure consists of the following steps:

1) The vertical profiles of air temperature $T(z)$ and relative humidity $f(z)$ were defined by analyzing the radiosounding measurements performed at the TNB station, during the measurement periods relative to the three OASI datasets. These data were analyzed following the correction procedure developed by Tomasi et al. (2006) for sets of radiosounding measurements taken at Dome C, in which (i) the Wang et al. (2002) algorithms were used to correct various dry bias errors, (ii) the solar heating dry bias effects were evaluated according to Turner et al. (2003) and Miloshevich et al. (2006), and (iii) further smoothing and lag error correction procedures were applied (Miloshevich et al. 2004).
2) The vertical profiles of absolute humidity $q(z)$ were then calculated at numerous fixed tropospheric levels from those of $T(z)$ and $f(z)$ defined above, in terms of the well-known equation of state for water vapor.
3) The above vertical profiles were completed up to the 30-km height with the average profiles defined by models OASI-A, OASI-B, and OASI-C.
4) Precipitable water W was calculated for each radiosounding, by integrating the vertical profile of $q(z)$ from the surface up to 30 km.
5) The daily time patterns of surface absolute humidity q_o measured at the Eneide station were determined by calculating this quantity in terms of the well-known equation of state for water vapor, using the values of temperature T_o and relative humidity f_o measured at the Eneide station.
6) The surface values of absolute humidity q_{Io} were then calculated at all the sun photometer measurement times by linear interpolation in time between the Eneide values of q_o determined at the previous point.
7) The value of scale height H_s was determined for each radiosounding by simply dividing the corresponding value of W found at step 4 by the simultaneous value of q_o, as calculated at step 5, since the radiosounding station is close to the Eneide station and at a very close altitude.
8) The time patterns of H_s were defined as ratios W/q_o,

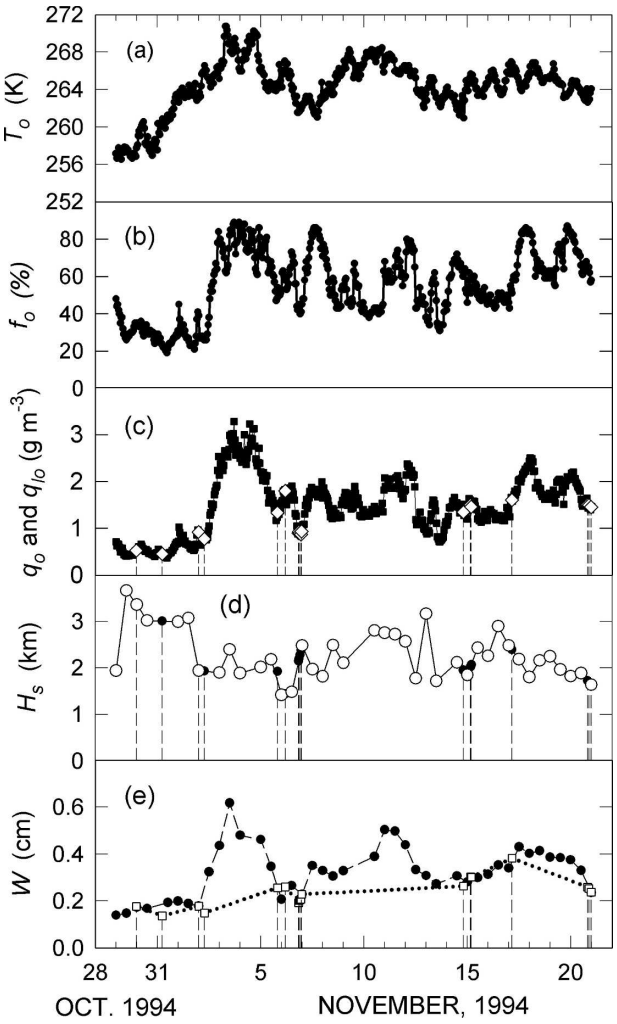

FIG. A1. Example of application of the PWIT procedure to dataset B taken at the OASI site in late Oct and Nov 1994: (a) time patterns of the hourly values of surface temperature T_o measured at the Eneide meteorological station, from 29 Oct to 20 Nov 1994; (b) time patterns of relative humidity f_o measured at the Eneide station; (c) time patterns of surface absolute humidity q_o (solid squares), measured at the Eneide station, and values of q_{Io} (open diamonds), obtained through linear interpolation in time between the values of q_o at the sun photometer measurement times (indicated by the dashed vertical lines); (d) time patterns of scale height H_s (open circles) for absolute humidity, determined as ratios W/q_o, and time patterns of linearly interpolated values of H_s in time (solid circles), for all the near-IR sun photometer measurement times; and (e) time patterns of precipitable water W determined from the TNB radiosoundings (solid circles), compared with the values of W (open squares) obtained as products of the linearly interpolated values in time of both H_s and q_{Io}, following the PWIT procedure.

with W measured at step 4 and q_o at step 5, from which the values of H_s were then derived through linear interpolation in time at the sun photometer measurement times.

9) The daily time patterns of W were finally defined by multiplying each value of H_s obtained at step 8 by the corresponding value of q_{Io} calculated at step 6 through linear interpolation in time between the values of q_o.

An example of the results found using the PWIT procedure, relative to the OASI-B dataset, is shown in Fig. A1. The two upper parts of the graph present the time patterns of T_o and f_o at the Eneide station, from which the time patterns of q_o were calculated, as shown in the third part of Fig. A1, where the values of q_{Io} were obtained by linear interpolation in time. The fourth part of Fig. A1 shows the time patterns of scale height $H_s = W/q_o$, where W was calculated through the integration procedure at step 4. The lowest part of Fig. A1 shows the comparison between the time patterns of W derived from the radiosoundings and those of the same quantity determined at all the sun photometer measurement times as products of the linearly interpolated values of H_s and q_{Io}, with relative errors ranging between 2% and 4%.

REFERENCES

Anderson, G. P., S. A. Clough, F. X. Kneizys, J. H. Chetwynd, and E. P. Shettle, 1986: AFGL Atmospheric Constituent Profiles (0-120 km). AFGL-TR-86-0110, 43 pp.

——, and Coauthors, 2000: MODTRAN4: Radiative transfer modeling for remote sensing. *Algorithms for Multispectral, Hyperspectral, and Ultraspectral Imagery VI,* S. S. Chen and M. R. Descour, Eds., International Society for Optical Engineering (SPIE Proceedings, Vol. 4049), 176–183.

Aonashi, K., T. Iwabuchi, Y. Shoji, R. Ohtani, and R. Ichikawa, 2004: Statistical study on precipitable water content variations observed with ground-based microwave radiometers. *J. Meteor. Soc. Japan,* **82,** 269–275.

Aristidi, E., and Coauthors, 2005: An analysis of temperatures and wind speeds above Dome C, Antarctica. *Astron. Astrophys.,* **430,** 739–746.

Bally, J., 1989: Atmospheric transparency over Antarctica from the mid-infrared to centimeter wavelengths. *Astrophysics in Antarctica,* D. J. Mullan, M. A. Pomerantz, and T. Stanev, Eds., AIP Press, 100–105.

Bartels, R. A., 1986: Comments on "Precipitable water measurements with sun photometers." *J. Climate Appl. Meteor.,* **25,** 1788–1790.

Bird, R. E., and R. L. Hulstrom, 1982: Precipitable water measurements with sun photometers. *J. Appl. Meteor.,* **21,** 1196–1201.

Burton, M. G., and Coauthors, 1994: The scientific potential for astronomy from the Antarctic Plateau. *Publ. Astron. Soc. Aust.,* **11,** 127–150.

Bussmann, R. S., W. L. Holzapfel, and C. L. Kuo, 2005: Millimeter wavelength brightness fluctuations of the atmosphere above the South Pole. *Astrophys. J.,* **622,** 1343–1355.

Calisse, P. G., M. C. B. Ashley, M. G. Burton, M. A. Phillips, J. W. V. Storey, S. J. E. Radford, and J. B. Peterson, 2004: Submillimeter site testing at Dome C, Antarctica. *Publ. Astron. Soc. Aust.,* **21,** 256–263.

Chiou, E.-W., M. P. McCormick, and W. P. Chu, 1997: Global

water vapor distributions in the stratosphere and upper troposphere derived from 5.5 years of SAGE II observations (1986–1991). *J. Geophys. Res.,* **102,** 19 105–19 118.

Curtis, A. R., 1952: Discussion of "A statistical model for water vapor absorption." *Quart. J. Roy. Meteor. Soc.,* **78,** 638–640.

Di Carmine, C., M. Campanelli, T. Nakajima, C. Tomasi, and V. Vitale, 2005: Retrievals of Antarctic aerosol characteristics using a Sun-sky radiometer during the 2001–2002 austral summer campaign. *J. Geophys. Res.,* **110,** D13202, doi:10.1029/2004JD005280.

Eldridge, R. G., 1967: Water vapor absorption of visible and near infrared radiation. *Appl. Opt.,* **6,** 709–713.

Gates, D. M., 1956: Infrared determination of precipitable water vapour in a vertical column of the Earth's atmosphere. *J. Meteor.,* **13,** 369–375.

——, and W. J. Harrop, 1963: Infrared transmission of the atmosphere to solar radiation. *Appl. Opt.,* **2,** 887–898.

Godson, W. L., 1955: The computation of infrared transmission by atmospheric water vapor. *J. Meteor.,* **12,** 272–284.

Goody, R. M., 1964: Band models. *Atmospheric Radiation I: Theoretical Basis, Oxford Monograph on Meteorology,* Oxford University Press, 122–170.

Gueymard, C. A., 2004: The sun's total and spectral irradiance for solar energy applications and solar radiation models. *Sol. Energy,* **76,** 423–453.

Harries, J. E., and Coauthors, 1996: Validation of measurements of water vapor from the Halogen Occultation Experiment (HALOE). *J. Geophys. Res.,* **101,** 10 205–10 216.

Iqbal, M., 1983: The solar constant and its spectral distribution. *An Introduction to Solar Radiation,* Academic Press, 44–50.

Kasten, F., 1966: A new table and approximation formula for the relative optical air mass. *Arch. Meteorol. Geophys. Bioklimatol.,* **B14,** 206–223.

Lahoz, W. A., and Coauthors, 1996: Vortex dynamics and the evolution of water vapour in the stratosphere of the Southern Hemisphere. *Quart. J. Roy. Meteor. Soc.,* **122,** 423–450.

Lawrence, J. S., M. C. B. Ashley, A. Tokovinin, and T. Travouillon, 2004: Exceptional astronomical seeing conditions above Dome C in Antarctica. *Nature,* **431,** 278–281.

Miloshevich, L. M., A. Paukkunen, H. Vömel, and S. J. Oltmans, 2004: Development and validation of a time-lag correction for Vaisala radiosonde humidity measurements. *J. Atmos. Oceanic Technol.,* **21,** 1305–1327.

——, H. Vömel, D. N. Whiteman, B. M. Lesht, F. J. Schmidlin, and F. Russo, 2006: Absolute accuracy of water vapor measurements from six operational radiosonde types launched during AWEX-G and implications for AIRS validation. *J. Geophys. Res.,* **111,** D09S10, doi:10.1029/2005JD006083.

Neckel, H., and D. Labs, 1984: The solar radiation between 3300 and 12500 Å. *Sol. Phys.,* **90,** 205–258.

Pitts, D. E., W. E. McAllum, M. Heidt, K. Jeske, J. T. Lee, D. DeMonbrun, A. Morgan, and J. Potter, 1977: Temporal variations in atmospheric water vapor and aerosol optical depth determined by remote sensing. *J. Appl. Meteor.,* **16,** 1312–1321.

Randel, W. J., F. Wu, A. Gettelman, J. M. Russell III, J. M. Zawodny, and S. J. Oltmans, 2001: Seasonal variation of water vapor in the lower stratosphere observed in Halogen Occultation Experiment data. *J. Geophys. Res.,* **106,** 14 313–14 326.

Rind, D., E.-W. Chiou, W. Chu, S. Oltmans, J. Lerner, J. Larsen, M. P. McCormick, and L. McMaster, 1993: Overview of the Stratospheric Aerosol and Gas Experiment II water vapor observations: Method, validation, and data characteristics. *J. Geophys. Res.,* **98,** 4835–4856.

Rosen, J. M., N. T. Kjome, and S. J. Oltmans, 1991: Balloon borne observations of backscatter, frost point and ozone in polar stratospheric clouds at the South Pole. *Geophys. Res. Lett.,* **18,** 171–174.

Thome, K. J., B. M. Herman, and J. A. Reagan, 1992: Determination of precipitable water from solar transmission. *J. Appl. Meteor.,* **31,** 157–165.

——, M. W. Smith, J. M. Palmer, and J. A. Reagan, 1994: Three-channel solar radiometer for the determination of atmospheric columnar water vapor. *Appl. Opt.,* **33,** 5811–5819.

Tomasi, C., and R. Guzzi, 1974: High precision atmospheric hygrometry using the solar infrared spectrum. *J. Phys. E: Sci. Instrum.,* **7,** 647–649.

——, V. Vitale, M. Tagliazucca, and L. Gasperoni, 1990: Infrared hygrometry measurements at Terra Nova Bay. *SIF Conf. Proc.,* **27,** 187–200.

——, A. Cacciari, V. Vitale, A. Lupi, C. Lanconelli, A. Pellegrini, and P. Grigioni, 2004: Mean vertical profiles of temperature and absolute humidity from a twelve-year radiosounding data set at Terra Nova Bay (Antarctica). *Atmos. Res.,* **71,** 139–169.

——, V. Vitale, B. Petkov, A. Lupi, and A. Cacciari, 2005: Improved algorithm for calculations of Rayleigh-scattering optical depth in standard atmospheres. *Appl. Opt.,* **44,** 3320–3341.

——, and Coauthors, 2006: Characterization of the atmospheric temperature and moisture conditions above Dome C (Antarctica) during austral summer and fall months. *J. Geophys. Res.,* **111,** D20305, doi:10.1029/2005JD006976.

Turner, D. D., B. M. Lesht, S. A. Clough, J. C. Liljegren, H. E. Revercomb, and D. C. Tobin, 2003: Dry bias and variability in Vaisala RS80-H radiosondes: The ARM experience. *J. Atmos. Oceanic Technol.,* **20,** 117–132.

Valenziano, L., and G. Dall'Oglio, 1999: Millimetre astronomy from the High Antarctic Plateau: Site testing at Dome C. *Publ. Astron. Soc. Aust.,* **16,** 167–174.

——, and Coauthors, 1998: APACHE96. CMBR anisotropy experiment at Dome C. *Proc. Astron. Soc. Pac.,* **141,** 81–89.

Vitale, V., and C. Tomasi, 1990: Atmospheric turbidity measurements at Terra Nova Bay with the multispectral sunphotometer model UVISIR. *SIF Conf. Proc.,* **27,** 89–104.

Volz, F. E., 1974: Economical multispectral sun photometer for measurements of aerosol extinction from 0.44 μm to 1.6 μm and precipitable water. *Appl. Opt.,* **13,** 1732–1733.

Walden, V. P., W. L. Roth, R. S. Stone, and B. Halter, 2006: Radiometric validation of the Atmospheric Infrared Sounder over the Antarctic Plateau. *J. Geophys. Res.,* **111,** D09S03, doi:10.1029/2005JD006357.

Wang, J., H. L. Cole, D. J. Carlson, E. R. Miller, K. Beierle, A. Paukkunen, and T. K. Laine, 2002: Corrections of humidity measurement errors from the Vaisala RS80 radiosonde—Application to TOGA COARE data. *J. Atmos. Oceanic Technol.,* **19,** 981–1002.

Westwater, E., Y. Han, M. Shupe, and S. Matrosov, 2001: Analysis of integrated cloud liquid and precipitable water vapor retrievals from microwave radiometers during the Surface Heat Budget of the Arctic Ocean project. *J. Geophys. Res.,* **106,** 32 019–32 030.

——, B. B. Stankov, D. Cimini, Y. Han, J. A. Shaw, B. M. Lesht, and C. N. Long, 2003: Radiosonde humidity soundings and microwave radiometers during Nauru99. *J. Atmos. Oceanic Technol.,* **20,** 953–971.